Bioorganic Chemistry 140 (2023) 106837

Contents lists available at ScienceDirect

Bioorganic Chemistry

journal homepage: www.elsevier.com/locate/bioorg

Cyclometalated iridium(III) complexes induce immunogenic cell death in HepG2 cells via paraptosis

Jiaxin Liao [a,1], Yuqing Zhang [a,1], Minying Huang [a,1], Zhijun Liang [a], Yao Gong [a], Ben Liu [a], Yuling Li [a], Jiaxi Chen [a,*], Wei Wu [a], Zunnan Huang [b,*], Jing Sun [a,b,*]

[a] School of Pharmacy, Guangdong Medical University, Dongguan 523808, China
[b] Key Laboratory of Computer-Aided Drug Design of Dongguan City, Guangdong Medical University, Dongguan 523808, China

ARTICLE INFO

Keywords:
Ir(III) complexes
Anticancer
Cytotoxicity
Paraptosis
ICD inducer
DC
Immunity
HepG2 cells
DAMPs
ER stress

ABSTRACT

Immunotherapy has been shown to provide superior antitumor efficacy by activating the innate immune system to recognize, attack and eliminate tumor cells without seriously harming normal cells. Herein, we designed and synthesized three new cyclometalated iridium(III) complexes (**Ir1**, **Ir2**, **Ir3**) then evaluated their antitumor activity. When co-incubated with HepG2 cells, the complex **Ir1** localized in the lysosome, where it induced paraptosis and endoplasmic reticulum stress (ER stress). Notably, **Ir1** also induced immunogenic cell death (ICD), promoted dendritic cell maturation that enhanced effector T cell chemotaxis to tumor tissues, down-regulated proportions of immunosuppressive regulatory T cells within tumor tissues and triggered activation of antitumor immunity throughout the body. To date, **Ir1** is the first reported iridium(III) complex-based paraptosis inducer to successfully induce tumor cell ICD. Furthermore, **Ir1** induced ICD of HepG2 cells without affecting cell cycle or reactive oxygen species levels.

1. Introduction

In the field of cancer therapy, the harnessing of the immune system to combat cancer is increasingly being evaluated as a promising emerging antitumor strategy [1]. The most well-known antitumor immune system-harnessing agents include immune checkpoint inhibitors (ICIs) that target host immune cell surface molecules CTLA-4, PD-1 and PD-L1. ICIs act by blocking immune checkpoint functions and by stimulating tumor-specific *T*-cell immune responses that convert immune system effector cells into tumor-killing machines [2,3]. While ICI therapy has been shown to effectively combat multiple cancers, treatment efficacy varies substantially according to tumor type and can even vary between patients with the same type of malignancy [4,5]. As a result, traditional anticancer treatments, such as surgery, radiation and chemotherapy, continue to be viewed as clinical best practices in some countries.

Early researchers in the field of ICI therapy, Casares and colleagues, demonstrated that the anthracycline doxorubicin supported the generation of an immune response within tumors in the absence of any adjuvant [6]. More recently, oxaliplatin was found to promote ICD by exposing calreticulin (CRT) molecules on tumor cell surfaces while also triggering extranuclear release of high-mobility group box 1 protein (HMGB-1) [7]. Notably, ICD was defined by the Nomenclature Committee on Cell Death (NCCD) in 2020 as a stress-induced regulatory cell death (RCD)-related process that, under certain circumstances, can cause the body's inflammatory response to induce adaptive cytotoxic T lymphocyte (CTL)-mediated immunity and long-term immunological memory. Interestingly, it has been demonstrated that certain drugs can kill tumor cells, while also invoking ICD by activating an immune response within the tumor microenvironment. Based on this premise, researchers are increasingly developing and evaluating new chemotherapeutic agents for use in combination with tumor immunotherapies, with ICDs performing both functions[8–10]. Nevertheless, in clinical practice only a small number of ICD-inducing chemotherapeutic agents have been identified, including adriamycin[11,12], mitoxantrone[13] and cyclophosphamide[14], as well as the aforementioned agents doxorubicin and oxaliplatin.

As non-platinum metal complexes, iridium(III) complexes, have increasingly attracted the attention of researchers, due to their excellent antitumor activities and remarkable luminescent features[15,16].

* Corresponding authors at: School of Pharmacy, Guangdong Medical University, Dongguan 523808, China (J. Sun).
E-mail addresses: jiaxi@gdmu.edu.cn (J. Chen), zn_huang@gdmu.edu.cn (Z. Huang), sunjing@gdmu.edu.cn (J. Sun).
[1] Contributed equally to this work.

https://doi.org/10.1016/j.bioorg.2023.106837
Received 10 July 2023; Received in revised form 25 August 2023; Accepted 3 September 2023
Available online 7 September 2023

Encouragingly, results of early studies revealed that Ir(III) complexes targeted the endoplasmic reticulum (ER) to kill tumor cells via apoptosis, while also acting as immunomodulating adjuvants to promote tumor cell killing via ICD[17]. Similarly, results of the current study suggest that Ir(III) complexes target the ER to induce an obvious ICD effect. However, our results also indicated that tumor cell ICD was accompanied by Ir(III) complex targeting of mitochondria and lysosomes with unknown antitumor effects, which is of great significance, since Ir(III) complexes that target lysosomes to induce ICD and chemotherapeutic agents that induce both cancer cell paraptosis and ICD have not yet been reported.

In this work, three cyclometalated Ir(III) complexes, **Ir1**, **Ir2** and **Ir3**, were designed, synthesized and evaluated to serve as antitumor agents (Fig. 1). Thereafter, **Ir1** lysosome-specific targeting, cellular uptake and cytotoxic effects on a non-tumor cell-derived cell line and various types of cancer cells were studied, with results showing that the **Ir1** anticancer mechanism of action involved caspase-independent paraptosis. Moreover, results obtained from additional studies conducted using HepG2 cells indicated that **Ir1** induced ER stress and also triggered ICD by uncovering CRT on tumor cell surfaces while also promoting extracellular HMGB-1 release and substantial ATP secretion. Furthermore, injection of **Ir1**-treated homologous tumor cells into C57BL/6 mice significantly prevented growth of transplanted tumor *in vivo*.

2. Results and discussion

2.1. Synthesis of Ir(III) complexes and characterization of their photophysical properties

Ligand L (2-(quinoxalin-6-yl)-1H-imidazo[4,5-f][1,10]phenanthroline) was prepared as follows: 1,10-phenanthroline-5,6-dione, glacial acetic acid and ammonium acetate were added to a reaction flask then the mixture was refluxed until all solutes were dissolved. Thereafter, the reaction was initiated by adding quinoxalin-6-carboxaldehyde to the solution then the mixture was refluxed until the solid in the flask was completely dissolved. Next, the pH of the solution was adjusted to 7, resulting in precipitation of a solid product that was subsequently washed with water and ethanol then dried to generate L. Thereafter, complexes **Ir1**-**Ir3** were synthesized by reacting two equivalents of L with one equivalent of Ir(III) chloro-bridged dimer using similar synthetic routes to generate the three complexes, as presented in Scheme S2. Results of elemental analysis, ESI-MS and ^{1}H NMR of ligand L and the three complexes are presented in Fig. S1-S8; All compounds (L, **Ir1**-**Ir3**) are >95% pure by HPLC analysis (Fig. S9-S12). UV–Vis absorption spectra of **Ir1**-**Ir3** in PBS, CH_3CN and CH_2Cl_2 are shown in Fig. S13. The main absorption band observed within the absorbance wavelength range of 320–380 nm corresponds to the internal electron transition of the ligands, while the weak absorption band within the absorbance wavelength range of 395–420 nm belongs to the metal-to-ligand charge transfer transition[18]. When excited by light of wavelength 405 nm, all three complexes emitted light in PBS, CH_3CN, and CH_2Cl_2 at 298 K (Fig. S14). Measurements of oil–water partition coefficients for **Ir1**-**Ir3** using the shaker flask method provided log*Po/w* values for the complexes that were ranked in decreasing order as **Ir1** (1.71) > **Ir3** (1.45) > **Ir2** (0.32).

2.2. Antitumor activities and cellular locations of complexes in vitro

Five human cancer cell lines and five murine cancer cell lines were evaluated via 3-(4,5-dimethylthiazol-2-yl)-2,5-diphenyl-2H-tetrazolium bromide (MTT) assays in order to assess *in vitro* effects of ligand L, the three complexes and the cisplatin (CDDP) on cell viability (Table S1). Based on MTT assay results, all three complexes exhibited excellent antitumor activity against cancer line cells. Notably, **Ir2** (IC_{50}: 1.6 ~ 3.3 μM) and **Ir3** (IC_{50}: 1.8 ~ 6.2 μM) exhibited greater cytotoxicity towards all tumor cell types as compared to corresponding effects of **Ir1** (IC_{50}: 4.2 ~ 37.4 μM). However, **Ir1** (IC_{50}: 24.4 ± 0.2 μM) was less toxic to non-tumorigenic L02 cells than **Ir2** (IC_{50}: 2.1 ± 0.2 μM) and **Ir3** (IC_{50}: 4.3 ± 0.4 μM). This result prompted us to select **Ir1** for further investigation, since **Ir1** would likely be less cytotoxic to normal cells than to tumor cells (e.g. HepG2 cells) and thus would provide superior selectivity for HepG2 cells *vs.* non-tumorigenic cells in *in vitro* assays.

Cyclometallic Ir(III) complexes have rich optical properties that allow their intracellular distributions to be tracked using fluorescence microscopy[19]. As shown in Fig. S15A and Fig. S15B, **Ir1** completely entered the cytoplasm during the 6-h co-incubation with HepG2 cells. Meanwhile, co-staining of **Ir1**-treated cells with mitochondrial MTR probe (MitoTracker® Green) and lysosomal LTR probe (LysoTracker® Green), revealed **Ir1**-associated red fluorescence that overlapped negligibly with the green fluorescence emitted by the mitochondrial

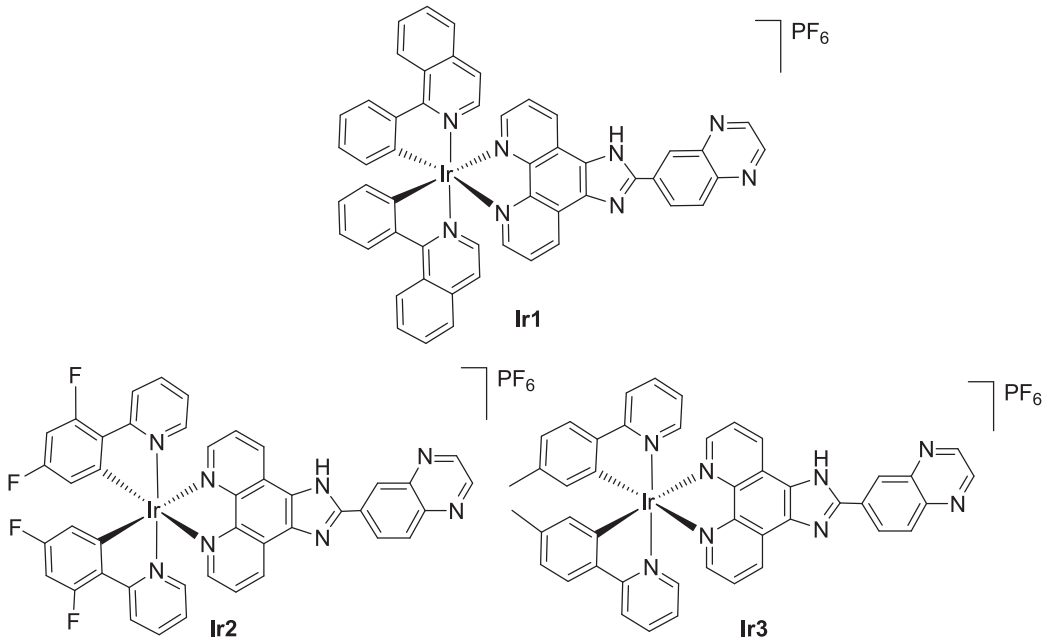

Fig. 1. Molecular structure of complexes **Ir1**-**Ir3**.

probe (PCC = 0.368) and overlapped significantly with the green fluorescence emitted by the lysosomal probe (PCC = 0.842). Thus, after entering HepG2 cells, **Ir1** mainly entered the cytoplasm then entered lysosomes. Investigation of this process using a cellular uptake assay revealed that the amount of **Ir1** entering cells was reduced at low temperature (4 °C) or in the presence of the metabolic inhibitor carbonyl cyanide 3-chlorophenylhydrazone (CCCP), but was not affected by the presence of chloroquine, an endocytosis inhibitor (Fig. S15C). Taken together, these results indicate that **Ir1** entered cells via an energy-dependent mechanism.

2.3. Investigation of the cell death mechanism of Ir1

Medication-induced apoptosis is often accompanied by the triggering of a series of biochemical processes[20,21]. **Ir1**-induced nuclear morphological changes did not exhibit typical apoptosis features, including fragmented nuclei, plasma membrane blebbing and apoptotic bodies (Fig. 2A). In order to rule out apoptosis as an **Ir1** cell death mechanism, Annexin V staining assays were conducted to detect cellular phosphatidylserine externalization, a recognized marker of early apoptosis. As compared to results obtained for control cells, only a negligible change in the proportion of membrane-linked protein V-positive cells was observed after cells were treated with **Ir1** (Fig. 2B). In addition, due to the fact that caspase activation is considered a key biochemical indicator of apoptosis, caspase-3 and poly(ADP-ribose) polymerase-1 (PARP) activation in cells treated with CDDP or **Ir1** were assessed via protein blot analysis. The results of this analysis revealed activation of both caspase-1 and PARP enzymes by CDDP, while no alterations in activation states of these enzymes in **Ir1**-treated cells were observed (Fig. 2C), thus demonstrating that **Ir1**-induced cell death did not occur via a conventional apoptotic process. Moreover, **Ir1** treatment exerted no cell cycle-associated effects (Fig. S16 and Table S2).

Unlike apoptosis, paraptosis-induced cell death is characterized by the production of sizable cytoplasmic vacuoles[22]. After cells were treated with **Ir1**, the internal cellular structure was examined via light microscopy and transmission electron microscopy (TEM). As shown in Fig. 3A and Fig. 3B, cytoplasmic vacuoles appeared, of which some contained large amounts of unfolded proteins and others contained debris resembling broken mitochondrial ridges that were accompanied by enlarged ER and mitochondrial structures. Previous studies have identified certain ICD inducers that can cause mitochondrial swelling when treating Hepatocellular carcinoma[23,24]. Taken together, these results suggest that **Ir1** promoted paraptosis in HepG2 cells.

Reactive oxygen species (ROS) are intracellular intermediates produced by the mitochondrial respiratory chain during normal aerobic metabolism, as well as in cells treated with most known chemotherapeutic agents, which exert their antitumor effects by promoting intracellular ROS production causes excessive tumor cell oxidative damage and functional abnormalities[25–27]. In this study, the fluorescent probe 2′,7′-dichlorodihydrofluorescein diacetate (DCFH-DA) was used to detect ROS levels in **Ir1**-treated cells. Surprisingly, green fluorescence was very weak in **Ir1**-treated cells, while flow cytometric quantification of intracellular ROS levels revealed that with increasing **Ir1** concentration, intracellular ROS intensity decreased considerably to levels that were even lower than corresponding control group levels (Fig. S17). In general, moderate intracellular amounts of ROS are required by normal cells to sustain cellular processes, such as tissue homeostasis, cell differentiation and proliferation and regulation of intracellular and extracellular signaling[28]. However, excessive inhibition of ROS production leads to disruption of intracellular phosphorylation, dephosphorylation and disruption of redox homeostasis that cause intracellular dysfunction and eventual cell death. Meanwhile, studies have shown that production of giant mitochondria is induced when cells are exposed to various types

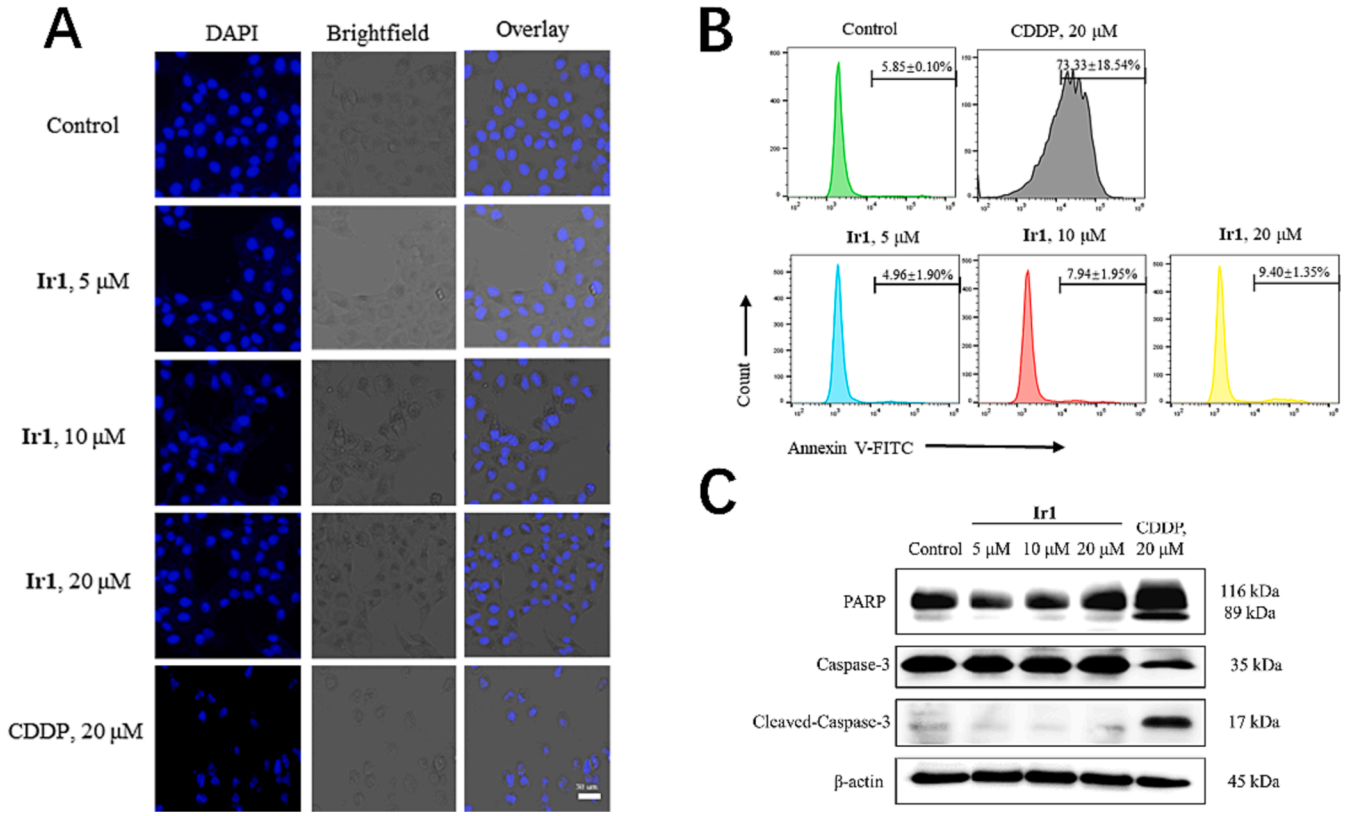

Fig. 2. (A) Confocal microscopy analysis of morphological alterations of HepG2 cells treated with CDDP (20 μM) and different concentration of **Ir1** (5, 10 and 20 μM) for 24 h. Cells were stained with DAPI. (B) Flow cytometric quantification of annexin V single labeled HepG2 cells were treated with **Ir1** and CDDP for 24 h. (C) Western blot analysis of PARP, Caspase-3 and Cleaved Caspase-3 proteins.

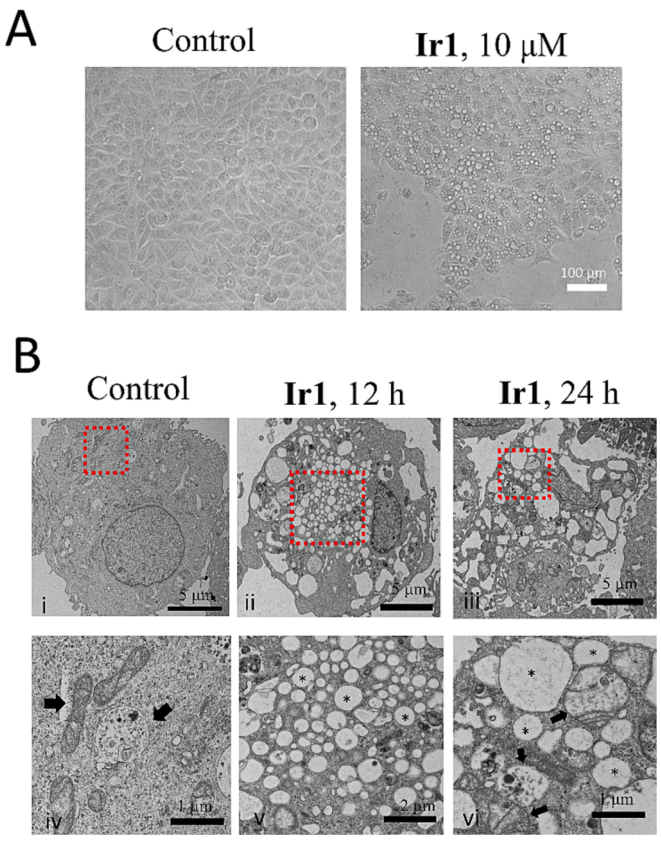

Fig. 3. (A) Light microscopy images of HepG2 cells treated with 10 μM **Ir1**. (B) The representative TEM images explaining the morphological features of HepG2 cells treated with **Ir1** (10 μM) for 12 h and 24 h.

of free radicals[29]. In turn, free radicals alter mitochondrial membrane biochemical properties, resulting in reduced oxygen consumption, phosphorylation capacity and intracellular ROS levels. As shown in Fig. 3B, intracellular mitochondria of **Ir1**-treated cells appeared swollen and damaged, with broken membrane ridges observed. This result indicated that observed reduced intracellular ROS levels after **Ir1** treatment may have been caused by giant mitochondria production, as consistent with reported effects of paraptotic agents[30].

2.4. In vitro ICD studies

Cells undergoing paraptosis exhibit calcium level imbalances and ROS-related mitochondrial dysfunction[31], as well as disruption of key ER functions associated with Ca^{2+} storage, protein folding and post-translational modification[32,33]. Importantly, ER stress occurs when cells are damaged or endostasis becomes imbalanced[34]. To assess cellular ER stress, **Ir1**-treated and untreated cells were stained with Fluo-3 AM, a probe commonly used to monitor intracellular Ca^{2+} levels [35]. Staining results revealed that in **Ir1**-treated cells, cellular fluorescence was mainly concentrated in the ER as an indication that Ca^{2+} had been released from the ER into the cytoplasm, which is a sign of severe ER stress (Fig. 4A). Meanwhile, C/EBP-homologous protein (Chop) and eukaryotic initiation factor 2α (eIF2α) levels were monitored in cells treated with various **Ir1** concentrations via western blotting. As seen in Fig. 4B, over-expression of Chop and phosphorylation of eIF2α (p-eIF2α), which are both signatures of ER stress[36–38], were observed after **Ir1** treatment.

Cells undergoing ICD can activate tumor-specific immune responses by releasing molecules known as damage-associated molecular patterns (DAMPs). DAMPs support long-term efficacy of anticancer drugs via two mechanisms: through direct killing of cancer cells and through induction of antitumor immunity[39,40]. In general, cell surface membrane CRT expression[41], HMGB-1 translocation outside the nucleus[42] and extracellular adenosine triphosphate (ATP) release are major ICD features that can be used to distinguish ICD from other tumor cell-killing mechanisms[43].

It has been reported that CRT protein, a highly conserved calcium-binding protein located primarily in the ER that maintains Ca^{2+} homeostasis, can be transferred from the ER lumen to the cell membrane surface during early stages of ICD development[44,45]. Here, cell surface CRT protein was detected after cells were treated with different **Ir1** concentrations. As shown in Fig. 4C, green fluorescence observed at the cell surface gradually increased with increasing **Ir1** concentration, which indicated that **Ir1** was able to induce CRT transfer to the cell membrane surface, while no fluorescence was observed in the vehicle-treated group. Due to the fact that tumor cells in late-stage ICD can promote DCs maturation by releasing HMGB-1 and by stimulating DCs presentation of tumor antigens to T cells[46], HMGB-1 protein content in extracellular fluid was monitored here using ELISAs (Fig. 4D). From the results, it can be seen that 10 μM **Ir1** treatment of HepG2 cells triggered release from cells of a peak amount of HMGB-1, while the amount of HMGB-1 released from cells treated with 20 μM **Ir1** was much lower. Due to the fact that ATP is a direct energy source for cells, release of ATP from cells in an advanced ICD state can activate and recruit inflammatory pathway-associated antigen-presenting cells (APCs) to enhance immune system activity[47]. In this study, we used a chemiluminescence kit to detect ATP content of extracellular fluid (Fig. 4E) and found that incubation of cells with 10 μM **Ir1** was associated with greatest extracellular ATP content. Collectively, the abovementioned results indicate that 10 μM **Ir1** treatment was associated with greatest ICD induction.

At the same time, ICD induction experiments were performed using cells of the Hepa1-6 cell line, which are derived from murine hepatocellular carcinoma cells. As compared to CDDP-treated Hepa1-6 cells, Hepa1-6 cells treated with 15 μM **Ir1** exhibited significant ICD characteristics, including significantly increased cell surface CRT overexpression, extranuclear release of HMGB-1 and extracellular ATP release. In addition, results of Fluo-3 AM calcium probe-based assays and protein immunoblotting assays indicated that ER stress occurred in Hepa1-6 cells after treatment with 15 μM **Ir1** (Fig. 5A-Fig. 5E).

Expression of CD86 and CD80 molecules on cell surfaces of bone marrow-derived dendritic cells (BMDCs) are used to confirm DC maturity. In this study, bone marrow cells were extracted using the Lutz method then relevant growth-stimulating factors were added to stimulate differentiation of BMDCs into DC cells, which was confirmed via flow cytometric analysis of cell surface CD80 and CD86 levels. Thereafter, Hepa1-6 cells and BDMCs were incubated with various **Ir1** concentrations followed by flow cytometric assessments of CD80 and CD86 levels. The results of these experiments revealed that Hepa1-6 cells pretreated with 5 μM **Ir1** exhibited greater cell surface expression of CD80 as compared to untreated control cells. Meanwhile, BDMCs treated with 15 μM **Ir** expressed both CD86 and CD80 on cell surfaces in large amounts. However, cell surface amounts of CD80 decreased when cells were treated with 30 μM **Ir1**, indicating that CD80 expression was weakened at higher **Ir1** concentrations. Taken together, these results suggest that excessive **Ir1** not only led to rapid death of Hepa1-6 cells, but also attenuated the ICD effect (Fig. 5F).

2.5. In vivo antitumor immunity

To investigate *in vivo* antitumor activity of **Ir1**, we chose C57BL/6 mice with natural immunity rather than immunodeficient nude mice. Hepa1-6 cells treated with 15 μM **Ir1** or 20 μM CDDP for 24 h served as "vaccines" that were injected subcutaneously into mice, while mice in the control group were injected with Hepa1-6 cells treated for 24 h with PBS solution. On the seventh day after vaccination (day 0), small pieces of tumor tissue were transplanted into the right leg of each mouse then

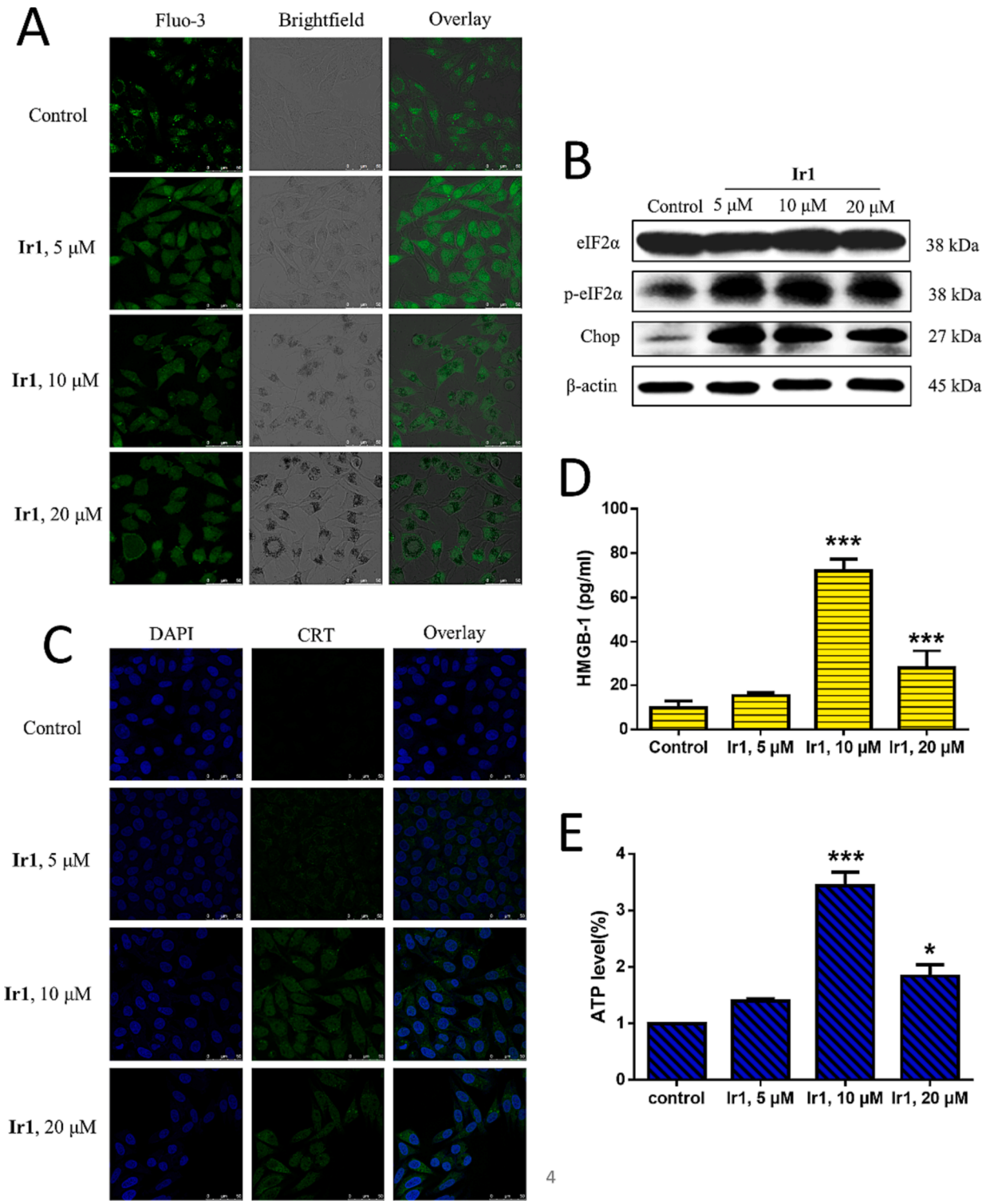

Fig. 4. (A) Confocal images of intracellular Ca^{2+} in HepG2 cells treated with **Ir1** (5, 10 and 20 μM) for 12 h, stained with Fluo-4 AM. (B) Western blot analysis of eIF2α, p-eIF2α and Chop proteins. (C) Confocal images of CRT on the surface of HepG2 cells treated with **Ir1** in different concentrations. (D) ELISA analysis of HMGB-1 in HepG2 cell supernatant treated with **Ir1** in different concentrations. (E) Analysis of ATP levels in cell supernatant of different concentrations of **Ir1**-treated HepG2 cell. (***$p < 0.001$, **$p < 0.01$, *$p < 0.05$).

on day 16, six mice from each group were euthanized then spleen and tumor tissues were harvested (Fig. 6A). Notably, the mean tumor volume of the CDDP group was lower than that of the control group, suggesting that CDDP may have triggered an immune effect that inhibited tumor growth. Meanwhile, the mean tumor volume of the **Ir1** group increased slowly for 10 days after tumor transplantation then plateaued thereafter. On day 30, after the remaining mice were photographed from the back and side (Fig. S18), they were euthanized then their tumor masses were removed. As shown in Fig. 6B and Fig. 6C, the **Ir1** group mean tumor mass did not increase and even decreased after treatment, while tumors grew rapidly along inguinal sides of mice in the control group. By contrast, tumors in the CDDP group were slightly smaller than

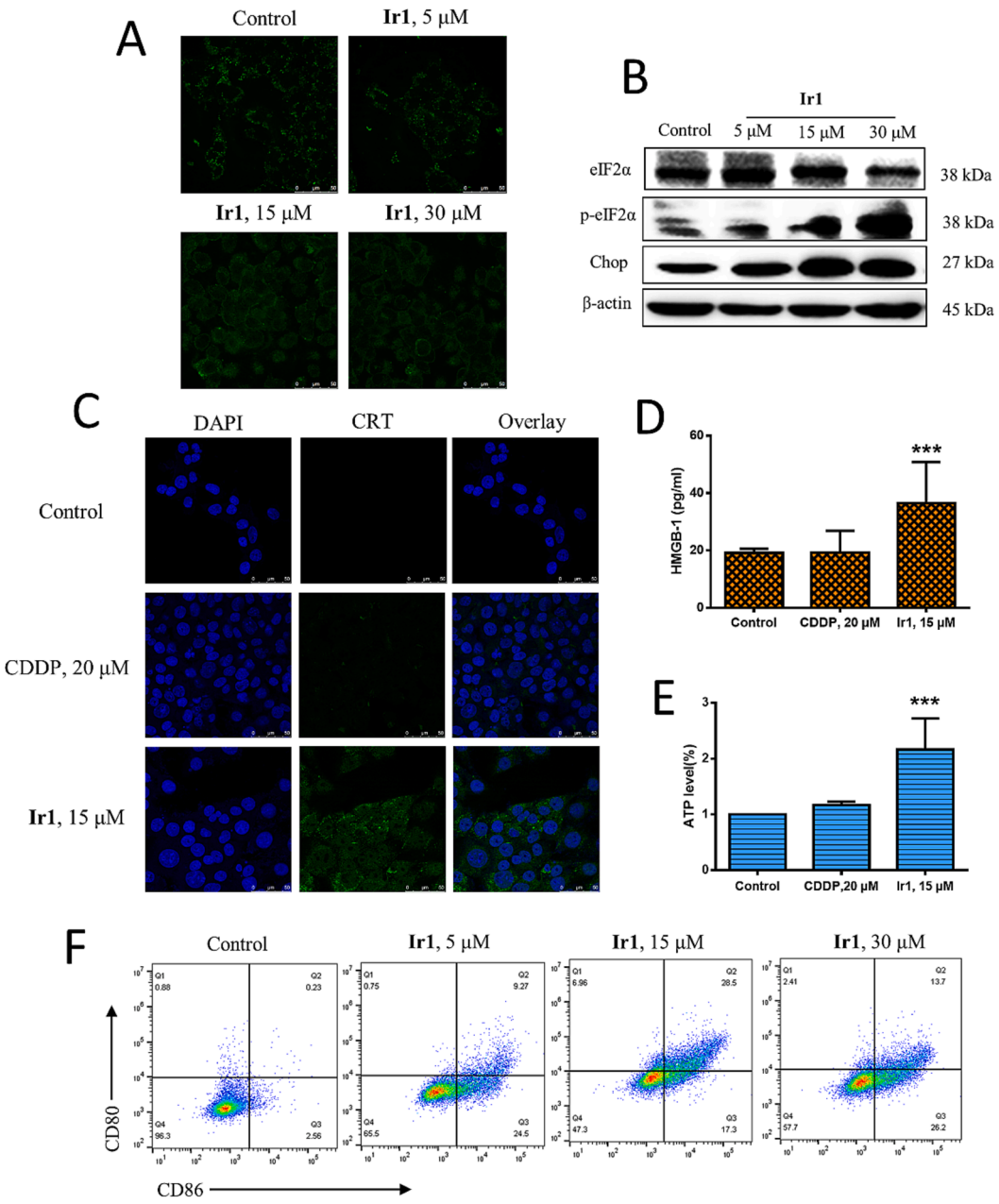

Fig. 5. (A) Confocal images of intracellular Ca^{2+} in Hepal-6 cells treated with **Ir1** (5, 15 and 30 μM) for 12 h, stained with Fluo-4 AM. (B) Western blot analysis of eIF2α, p-eIF2α and Chop proteins. (C) Confocal images of CRT on surface of Hepal-6 cells treated with **Ir1** (15 μM) and CDDP (20 μM) Hepa1-6 cells. (D) ELISA analysis of HMGB-1 in cell supernatant of **Ir1**-treated (15 μM) and CDDP-treated (20 μM) Hepa1-6 cells. (E) Analysis of ATP levels in cell supernatant of **Ir1**-treated (15 μM) and CDDP-treated (20 μM) Hepa1-6 cells. (F) Flow cytometric quantification of BMDC maturation in Hepa1-6 cells after co-culture with **Ir1** (5, 15 and 30 μM) for 24 h. (***$p < 0.001$).

those of the control group, but were significantly larger than those of the **Ir1** group. In addition, **Ir1** treatment did not lead to significant mortality or remarkable changes in body weight among the experiment (Fig. 6D). Furthermore, H&E staining of paraffin-embedded sections of heart, liver, spleen, lung and kidney tissues revealed no obvious lesions in tissues of Ir1 group mice. Taken together, these results indicate that **Ir1** was not toxic to surrounding organs (Fig. 6E).

In order to assess **Ir1** effects on *in vivo* immune system function, proportions of DC cells and T cells belonging to different T cell subsets in spleen and tumor tissues after 16 days of tumor transplantation was examined via flow cytometric analysis. The results indicated that the proportion of splenic DCs ($CD11c^+$ cells) was significantly greater in the **Ir1** group (5.56 ± 1.25%) than in the control group (3.10 ± 0.79%), while a slight increase in splenic DC proportion was observed in the CDDP group (4.01 ± 0.64%). It is noteworthy that the proportion of immunosuppressive regulatory T cells (T_{reg} cells) in spleens of mice was elevated in the CDDP group (1.34 ± 0.32%) as compared to the corresponding proportions of the other two groups (Control: 1.13 ± 0.01%, **Ir1**: 0.54 ± 0.01%). Proportions of T_{reg} cells, a subset of T cells that can significantly inhibit immune system activities, are significantly elevated in cancer patients[48,49] and appear to help tumor cells block normal immune surveillance to thereby enable immune escape[50,51]. In the CDDP group, the proportion of splenic T_{reg} cells was significantly greater than that of the control group, suggesting that immunosuppression may occur via multiple mechanisms. For example, immunosuppression observed in the CDDP group was not solely due to CDDP toxic effects on bone marrow cells, but may have also been caused by activities of $CD8^+$ T cells. $CD8^+$ T cells can act as cytotoxic T lymphocytes *in vivo* by

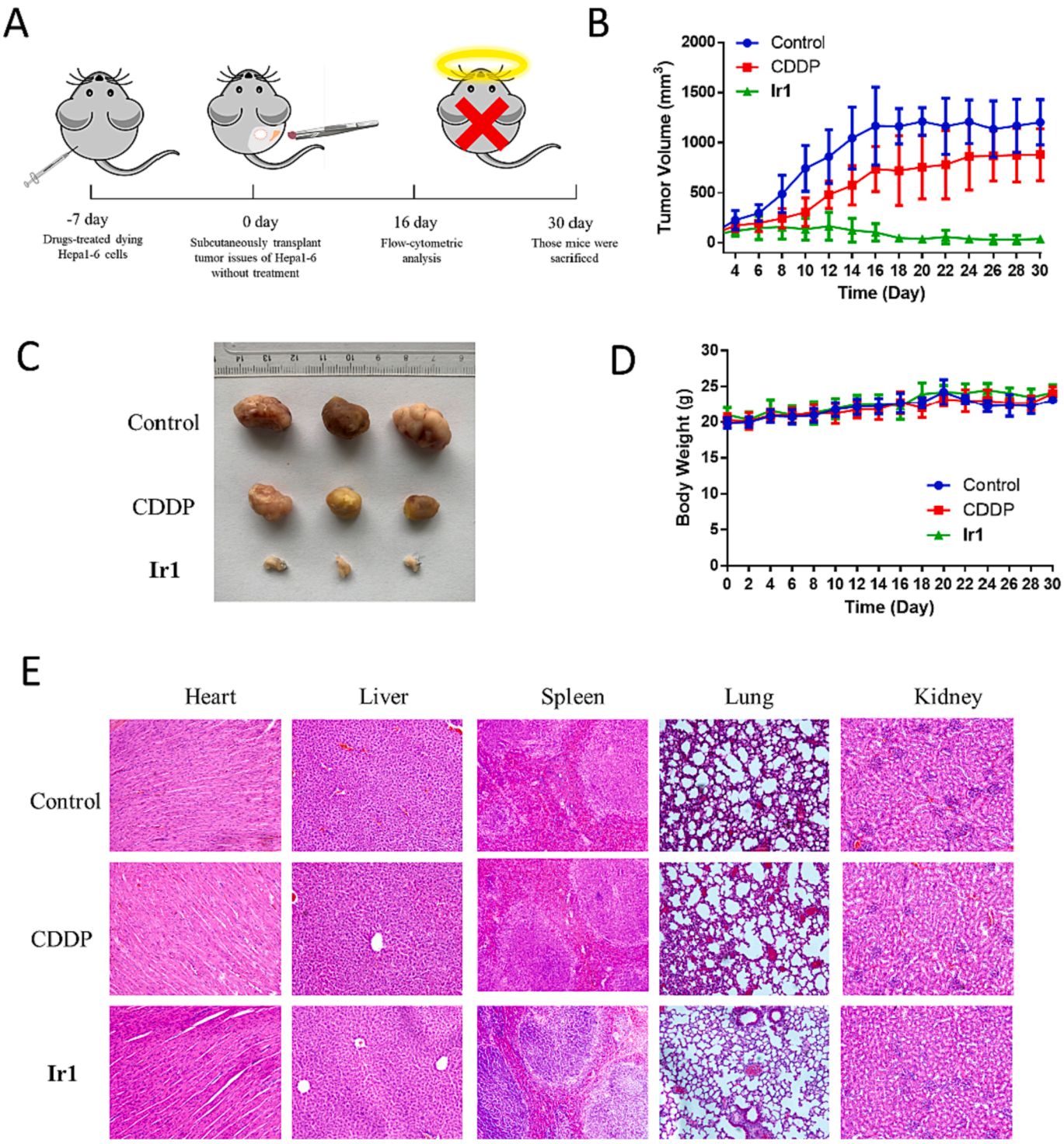

Fig. 6. (A) Schematic diagram of the ICD vaccine experiment. (B) The tumor volume growth curves of the mice in each group. (C) Photographs of tumors removed from the mice after treatment (30 days). (D) The weight of the mice throughout the follow-up period. (E) Histological examination of the main organs of the mice (30 days).

recognizing tumor antigens to thereby become activated tumor-killing effector cells via secretion of perforin, TNF-α and other immune factors[52,53]. In fact, the proportion of T_{reg} cells has been reported to be negatively correlated with the proportion of $CD8^+$ CTL cells, such that the $CD8^+$ T cell/T_{reg} cell ratio has been commonly used as a cancer patient clinical prognostic indicator[54]. Here the splenic $CD8^+$ T cell/T_{reg} cell ratio of the **Ir1** group (33.89%) was considerably higher than that of the control group (10.79%) and CDDP group (15.54%), thus indicating that treatment of tumor cells with **Ir1** enhanced immune system antitumor activity *in vivo* (Fig. S19 and Fig. 7A1-7F1).

In tumor tissues, proportions of DCs, $CD3^+$ T cells, $CD4^+$ T cells and $CD8^+$ T cells in the **Ir1** group (25.61 ± 3.36%, 86.99 ± 2.98%, 22.19 ± 1.59%, 11.29 ± 2.37%, respectively) were greater than corresponding control group proportions (8.38 ± 1.11%, 57.07 ± 11.50%, 3.47 ± 2.42%, 2.73 ± 1.29%, respectively) and CDDP group proportions (10.85 ± 1.24%, 68.67 ± 11.10%, 6.69 ± 4.01%, 6.42 ± 2.91%, respectively)

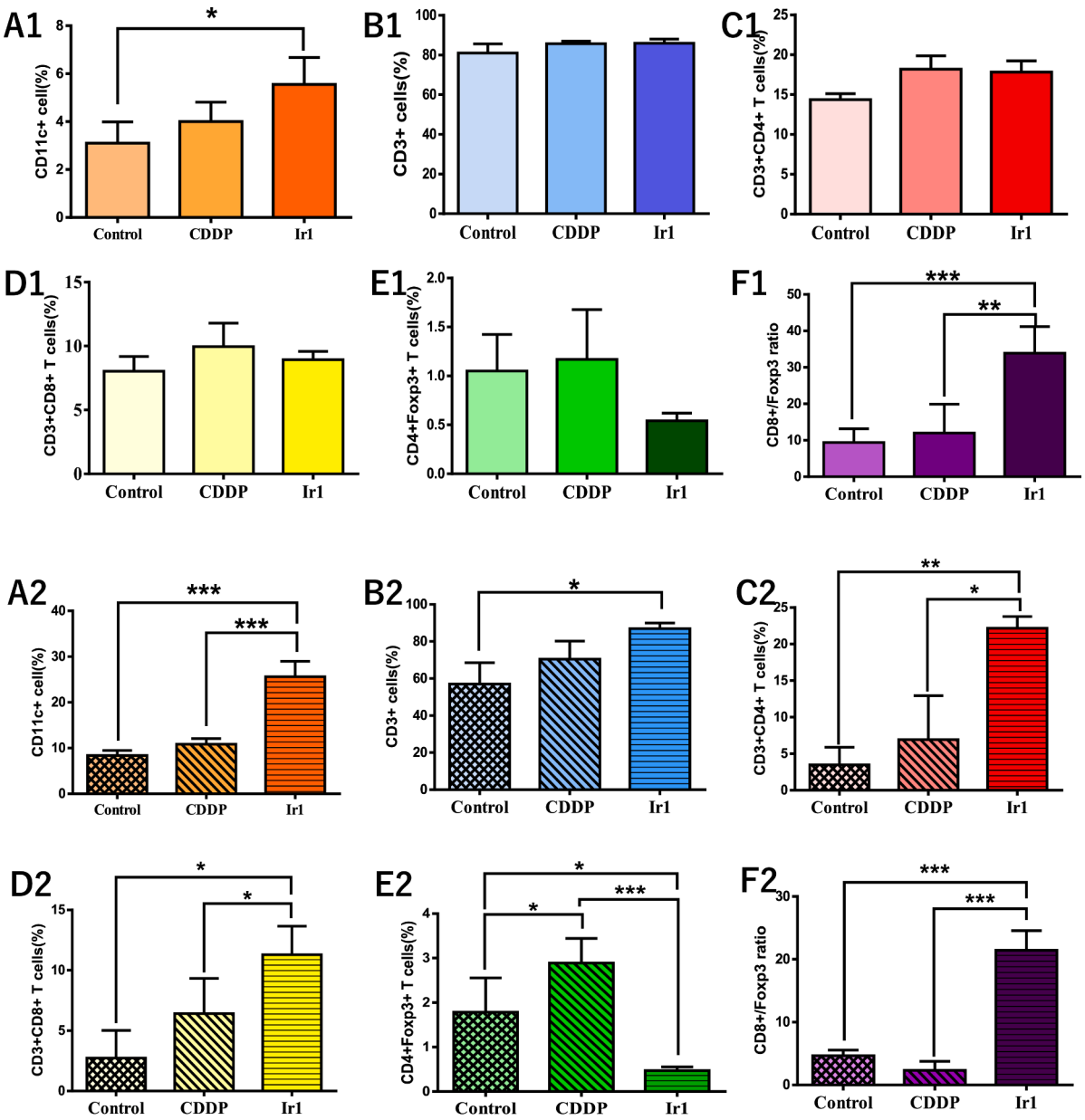

Fig. 7. Quantitative analysis by flow cytometry of the percentage of different cells in the spleen (A1-E1) and tumor (A2-E2). (A1, A2) DC, (B1, B2) $CD3^+$ T cell, (C1, C2) $CD3^+CD4^+$ T cell, (D1, D2) $CD3^+CD8^+$ T cell, (E1, E2) $CD4^+$Foxp3 cell, (F1, F2) $CD8^+$/Foxp3 ratio. (***$p < 0.001$, **$p < 0.01$, *$p < 0.05$).

(Fig. S20 and Fig. 7A2-7F2). Of these cell types, DCs and $CD4^+$ T cells were present in significantly greater proportions in the **Ir1** group than in the other groups, suggesting that **Ir1**-induced ICD effects could effectively enable these types of cells to recognize, chemotactically attract APCs, and enhance antigen presentation functions in response to immunologically recognized tumor antigens. The greater proportion of $CD8^+$ T cells in tumor tissues of the **Ir1** group *vs.* corresponding proportions of other groups indicates that **Ir1**-induced ICD significantly reduced tumor volumes or eradicated tumors by recruiting $CD8^+$ T cells and down-regulating T_{reg} cell activities. Comparisons of **Ir1** group T_{reg} cell proportions obtained for tumor tissues (0.47 ± 0.08%) revealed they were both lower than that of the control group (1.78 ± 0.77%), and were more markedly lower than that of the CDDP group (2.89% ± 0.55%). Therefore, the **Ir1**-induced ICD effect not only enhanced chemotactic activities of DCs and T cells in tumor tissues, but also reduced both the proportion of T_{reg} cells in the tumor microenvironment and the immunosuppressive effect observed in the cellular microenvironment.

3. Conclusion

In this study, three new cyclometalated Ir(III) complexes were synthesized, characterized and assessed for antitumor activities, which and were shown via MTT assays to be excellent for all three Ir(III) complexes. However, as compared to **Ir2** and **Ir3**, **Ir1** exhibited less cytotoxicity toward LO2 cells and was more selectively cytotoxic against cancer cells. Results of mechanistic investigations revealed that **Ir1** entered the cytoplasm and localized within lysosomes to induce tumor cell death via a mechanism that primarily involved paraptosis. In addition, **Ir1** was found to induce ER stress in HepG2 cells, which further enhanced the ICD effect (i.e., surface exposure of $CD8^+$ T cells and extracellular release of HMGB1 and ATP). Moreover, **Ir1** also promoted DCs maturation, enhanced chemotaxis of effector T cells to tumor tissue sites, alleviated immunosuppression by down-regulating the proportion of T_{reg} cells in tumor tissues, activated host immunity and ultimately immunized tumor-vaccinated mice against liver cancer tumors. Interestingly, **Ir1** did not cause an increase in cellular ROS, as has been

reported for other metal complexes with known ICD effects (e.g., oxaliplatin). Nonetheless, the unique antitumor activities and properties of the three Ir(III) complexes designed in this study provide a foundation to guide further development of Ir(III) complexes for use in inducing ICD.

To date, immunoregulatory functions of antitumor chemotherapeutic agents have not been systematically investigated. Here, we found that although CDDP did not induce an ICD effect, tumor growth was still inhibited in CDDP group mice after they received transplanted tumor cells. Thus, this result suggests that CDDP treatment induced immunomodulation, an effect that has never been reported before for CDDP. However, the proportion of T_{reg} cells within tumor tissues of CDDP group mice was markedly greater than that of the control group and thus reduced the $CD8^+$ T cell tumor-killing effect, warranting further study. Nevertheless, the results presented here highlight the importance of effects of chemotherapeutic agents on the immune response and thus may broaden the range of applications of these classical agents and open up new avenues for development of chemotherapeutics.

4. Experimental section

4.1. Synthetic protocol and characterization

4.1.1. Synthesis and characterization

$[Ir(piq)_2Cl]_2$[55], $[Ir(dfppy)_2Cl]_2$[56], and $[Ir(tpy)_2Cl]_2$[57] were prepared according to previously reported methods.

4.1.1.1. Synthesis of 2-(quinoxalin-6-yl)-1H-imidazo[4,5-f][1,10]phenanthroline (L). A mixture of 1,10-phenanthroline-5,6-dione (0.53 g, 2.5 mmol) and ammonium acid (3 g, 39 mmol) was dissolved in glacial acetic acid (80 mL) and stirred for 15 min at 60 °C. After the mixture dissolved, quinoxaline-6-formaldehyde (0.40 g, 2.5 mmol) was added and the solution refluxed for another 90 min at 100 °C. After the mixture was cooled to room temperature, ammonia was added to adjust the pH to neutral. Then, the yellow precipitate was precipitated, which was purified with water and absolute ethanol. Yield: 0.60 g (69.0%). Anal. Calcd for $C_{21}H_{12}N_6$ (348.11): C, 72.40; H, 3.47; N, 24.12. Found: C, 72.25; H, 3.43; N, 24.10. ESI-MS: $m/z = 349.0$ $[M+H^+]^+$. ^{1}H NMR (400 MHz, DMSO-d_6) δ 9.08–8.99 (m, 3H), 8.99–8.90 (m, 4H), 8.77 (dd, J = 8.7, 2.0 Hz, 1H), 8.27 (d, J = 8.8 Hz, 1H), 7.83 (dd, J = 8.1, 4.3 Hz, 2H), 1.88 (s, 1H).

4.1.1.2. Synthesis of $[Ir(piq)_2L]PF_6$ (Ir1). A mixture of L (0.18 g, 0.50 mmol, 2 equiv) and $[Ir(piq)_2Cl]_2$ (0.32 g, 0.25 mmol, 1 equiv) was prepared in 80 mL CH_2Cl_2/CH_3OH (2:1, *v/v*) by refluxing for 4 h under argon. After the solution has been cooled to room temperature, an appropriate amount of NH_4PF_6 was added and the stirring continued for 1 h. The pure product was gained after purification by column chromatography on silica gel diluted with CH_2Cl_2/CH_3OH (60:1, v/v). Yield: 0.16 g (29.3%). Anal. Calcd for $C_{51}H_{32}F_6IrN_8P$ (1094.20): C, 55.99; H, 2.95; N, 10.24. Found: C, 56.10; H, 2.31; 10.10. ESI-MS: $m/z = 949.0$ $[M-PF_6^-]^+$. ^{1}H NMR (400 MHz, DMSO-d_6) δ 9.23 (d, J = 8.5 Hz, 2H), 9.04 (dd, J = 19.0, 5.4 Hz, 5H), 8.82–8.78 (m, 1H), 8.40 (d, J = 8.1 Hz, 2H), 8.34 (d, J = 8.8 Hz, 1H), 8.04 (ddd, J = 10.0, 9.2, 3.6 Hz, 6H), 7.90–7.83 (m, 4H), 7.41 (dd, J = 13.0, 6.5 Hz, 4H), 7.17 (t, J = 7.6 Hz, 2H), 6.96 (t, J = 7.4 Hz, 2H), 6.29 (d, J = 7.6 Hz, 2H), 1.20 (s, 1H).

4.1.1.3. Synthesis of $[Ir(dfppy)_2L]PF_6$ (Ir2). **Ir2** was synthesized in a method similar to **Ir1**, except $[Ir(dfppy)_2Cl]_2$ (0.30 g, 0.25 mmol, 1 equiv) was used instead of $[Ir(piq)_2Cl]_2$. Yield: 0.18 g (33.8%). Anal. Calcd for $C_{43}H_{24}F_{10}IrN_8P$ (1066.13): C, 48.45; H, 2.27; N, 10.51. Found: C, 48.51; H, 2.20; N, 10.30. ESI-MS: $m/z = 921.0$ $[M-PF_6^-]^+$. ^{1}H NMR (400 MHz, DMSO-d_6) δ 9.24 (d, J = 7.9 Hz, 2H), 9.03 (d, J = 19.1 Hz, 3H), 8.77 (d, J = 9.8 Hz, 1H), 8.46–8.20 (m, 5H), 8.10 (s, 2H), 7.97 (s, 2H), 7.58 (s, 2H), 7.03 (d, J = 22.2 Hz, 4H), 5.72 (s, 2H), 1.20 (s, 1H).

4.1.1.4. Synthesis of $[Ir(tpy)_2L]PF_6$ (Ir3). **Ir3** was synthesized in a method similar to **Ir1**, except $[Ir(tpy)_2Cl]_2$ (0.28 g, 0.25 mmol, 1 equiv) was used instead of $[Ir(piq)_2Cl]_2$. Yield: 0.16 g (31.3%). Anal. Calcd for $C_{45}H_{32}F_6IrN_8P$ (1022.20): C, 52.89; H, 3.16; N, 10.96. Found: C, 52.76; H, 3.11; N, 11.02. ESI-MS: $m/z = 874.8$ $[M-PF_6^-]^+$. ^{1}H NMR (400 MHz, DMSO-d_6) δ 9.21 (d, J = 8.0 Hz, 2H), 9.13–8.87 (m, 3H), 8.78 (d, J = 8.7 Hz, 1H), 8.35 (d, J = 8.8 Hz, 1H), 8.29–8.17 (m, 4H), 8.11 (d, J = 5.1 Hz, 2H), 7.87 (t, J = 8.1 Hz, 4H), 7.50 (d, J = 5.6 Hz, 2H), 6.93 (dd, J = 16.8, 7.1 Hz, 4H), 6.11 (s, 2H), 2.12 (s, 6H), 1.22 (s, 1H).

Author contributions

J. X. Liao, Y. Q. Zhang and J. X. Chen designed, synthesized and characterized three Ir(III) complexes. J. X. Liao, Z. J. Liang, Y. Gong, Y. L. Li, B. Liu and W. Wu conducted the *in vitro* and *in vivo* experiments. Z. N. Huang and J. Sun performed the analysis of data. M. Y. Huang and J. Sun wrote the manuscript.

Declaration of Competing Interest

The authors declare that they have no known competing financial interests or personal relationships that could have appeared to influence the work reported in this paper.

Data availability

No data was used for the research described in the article.

Acknowledgments

This work was supported by the Discipline Construction Project of Guangdong Medical University (4SG22004G), Dongguan Science and Technology of Social Development Program (20211800905082), the Key Scientific Research Projects of Colleges and Universities in Guangdong Province (2020ZDZX2031), and Medical Industry Innovation Project of Guangdong Medical University (4SG22305P).

Appendix A. Supplementary data

Supplementary data to this article can be found online at https://doi.org/10.1016/j.bioorg.2023.106837.

References

[1] H.Z. Deng, W.J. Yang, Z.J. Zhou, R. Tian, L.S. Lin, Y. Ma, J.B. Song, X.Y. Chen, Targeted scavenging of extracellular ROS relieves suppressive immunogenic cell death, Nat. Commun. 11 (2020) 4951.
[2] C. Boutros, A. Tarhini, E. Routier, O. Lambotte, F.L. Ladurie, F. Carbonnel, H. Izzeddine, A. Marabelle, S. Champiat, A. Berdelou, E. Lanoy, M. Texier, C. Libenciuc, A.M. Eggermont, J.C. Soria, C. Mateus, C. Robert, Safety profiles of anti-CTLA-4 and anti-PD-1 antibodies alone and in combination, Nat. Rev. Clin. Oncol. 13 (2016) 473–486.
[3] E.I. Buchbinder, A. Desai, CTLA-4 and PD-1 pathways: similarities, differences, and implications of their inhibition, Am. J. Clin. Oncol. 39 (2016) 98–106.
[4] A. Rotte, Combination of CTLA-4 and PD-1 blockers for treatment of cancer, J. Exp. Clin. Canc. Res. 38 (2019) 255.
[5] A. Ribas, J.D. Wolchok, Cancer immunotherapy using checkpoint blockade, Science 359 (2018) 1350–1355.
[6] N. Casares, M.O. Pequignot, A. Tesniere, F. Ghiringhelli, S. Roux, N. Chaput, E. Schmitt, A. Hamai, S. Hervas-Stubbs, M. Obeid, F. Coutant, D. Métivier, E. Pichard, P. Aucouturier, G. Pierron, C. Garrido, L. Zitvogel, G. Kroemer, Caspase-dependent immunogenicity of doxorubicin-induced tumor cell death, J. Exp. Med. 202 (2005) 1691–1701.
[7] A. Tesniere, F. Schlemmer, V. Boige, O. Kepp, I. Martins, F. Ghiringhelli, L. Aymeric, M. Michaud, L. Apetoh, L. Barault, J. Mendiboure, J.P. Pignon, V. Jooste, P. van Endert, M. Ducreux, L. Zitvogel, F. Piard, G. Kroemer, Immunogenic death of colon cancer cells treated with oxaliplatin, Oncogene 29 (2010) 482–491.
[8] A. Ahmed, S.W.G. Tait, Targeting immunogenic cell death in cancer, Mol. Oncol. 14 (2020) 2994–3006.
[9] G. Kroemer, L. Galluzzi, O. Kepp, L. Zitvogel, Immunogenic cell death in cancer therapy, Annu. Rev. Immunol. 31 (2013) 51–72.

[10] N. Wang, Z. Wang, Z. Xu, X. Chen, G. Zhu, A cisplatin-loaded immuno-chemotherapeutic nanohybrid bearing immune checkpoint inhibitors for enhanced cervical cancer therapy, Angew. Chem. 57 (2018) 3426–3430.
[11] J.Q. Lu, X.S. Liu, Y.P. Liao, X. Wang, A. Ahmed, W. Jiang, Y. Ji, H. Meng, A.E. Nel, Breast cancer chemo-immunotherapy through liposomal delivery of an immunogenic cell death stimulus plus interference in the IDO-1 pathway, ACS Nano 12 (2018) 11041–11061.
[12] Z. Yu, J.F. Guo, M.Y. Hu, Y.Q. Gao, L. Huang, Icaritin exacerbates mitophagy and synergizes with doxorubicin to induce immunogenic cell death in hepatocellular carcinoma, ACS Nano 14 (2020) 4816–4828.
[13] W. Wei, H.B. Li, G.A. Zhang, Y. Zhang, K. Wu, R.R. Bao, G.G. Wang, H. Zheng, Y. Xia, C.L. Li, Proteasome inhibitors attenuates mitoxantrone-triggered immunogenic cell death in prostate cancer cells, Med. Oncol. 37 (2020) 116.
[14] M.X. Jiang, J. Zeng, L.Q. Zhao, M.G. Zhang, J.L. Ma, X.W. Guan, W.F. Zhang, Chemotherapeutic drug-induced immunogenic cell death for nanomedicine-based cancer chemo-immunotherapy, Nanoscale 13 (2021) 17218–17235.
[15] L.C. Lee, K.K. Lo, Luminescent and photofunctional transition metal complexes: from molecular design to diagnostic and therapeutic applications, J. Am. Chem. Soc. 144 (2022) 14420–14440.
[16] S. Sen, M. Won, M.S. Levine, Y. Noh, A.C. Sedgwick, J.S. Kim, J.L. Sessler, J. F. Arambula, Metal-based anticancer agents as immunogenic cell death inducers: the past, present, and future, Chem. Soc. Rev. 51 (2022) 1212–1233.
[17] L.L. Wang, R.L. Guan, L.N. Xie, X.X. Liao, K. Xiong, T.W. Rees, Y. Chen, L.N. Ji, H. Chao, An ER-targeting iridium(III) complex which induces immunogenic cell death in non-small cell lung cancer, Angew. Chem. 133 (2021) 4707–4715.
[18] B.B. Chen, N.L. Pan, J.X. Liao, M.Y. Huang, D.C. Jiang, J.J. Wang, H.J. Qiu, J. X. Chen, L. Li, J. Sun, Cyclometalated iridium(III) complexes as mitochondria-targeted anticancer and antibacterial agents to induce both autophagy and apoptosis, J. Inorg. Biochem. 219 (2021), 111450.
[19] V. Venkatesh, R. Berrocal-Martin, C.J. Wedge, I. Romero-Canelon, C. Sanchez-Cano, J.I. Song, J.P.C. Coverdale, P. Zhang, G.J. Clarkson, A. Habtemariam, S. W. Magennis, R.J. Deeth, P.J. Sadler, Mitochondria-targeted spin-labelled luminescent iridium anticancer complexes, Chem. Sci. 8 (2017) 8271–8278.
[20] L.E. Bröker, F.A.E. Kruyt, G. Giaccone, Cell death independent of caspases: a review, Clin. Cancer Res. 11 (2005) 3155–3162.
[21] M. Cini, H. Williams, M.W. Fay, M.S. Searle, S. Woodward, T.D. Bradshaw, Enantiopure titanocene complexes–direct evidence for paraptosis in cancer cells, Metallomics 8 (2016) 286–297.
[22] A. Binoy, D. Nedungadi, N. Katiyar, C. Bose, S.A. Shankarappa, B.G. Nair, N. Mishra, Plumbagin induces paraptosis in cancer cells by disrupting the sulfhydryl homeostasis and proteasomal function, Chem. Biol. Interact. 310 (2019), 108733.
[23] M.L. Bian, R. Fan, Z.B. Yang, Y.A. Chen, Z.R. Xu, Y.L. Lu, W.K. Liu, Pt(II)-NHC complex induces ROS-ERS-related DAMP balance to harness immunogenic cell death in hepatocellular carcinoma, J. Med. Chem. 65 (2022) 1848–1866.
[24] Z.B. Yang, M.L. Bian, L. Lv, X.Y. Chang, Z.F. Wen, F.W. Li, Y.L. Lu, W.K. Liu, Tumor-targeting NHC-Au(I) complex induces immunogenic cell death in hepatocellular carcinoma, J. Med. Chem. 66 (2023) 3934–3952.
[25] Z.R. Xu, J.Q. Xu, S.B. Sun, W. Lin, Y.M. Li, Q.Y. Lu, F.W. Li, Z.B. Yang, Y.L. Lu, W. K. Liu, Mecheliolide elicits ROS-mediated ERS driven immunogenic cell death in hepatocellular carcinoma, Redox Biol. 54 (2022), 102351.
[26] H. Yuan, Z. Han, Y.C. Chen, F. Qi, H.B. Fang, Z.J. Guo, S.R. Zhang, W.J. He, Ferroptosis photoinduced by new cyclometalated iridium(III) complexes and its synergism with apoptosis in tumor cell inhibition, Angew. Chem. 133 (2021) 8255–8262.
[27] N. Diwanji, A. Bergmann, An unexpected friend - ROS in apoptosis-induced compensatory proliferation: Implications for regeneration and cancer, Semin. Cell Dev. Biol. 80 (2018) 74–82.
[28] R. Mittler, ROS are good, Trends Plant Sci. 22 (2017) 11–19.
[29] J.N. Moloney, T.G. Cotter, ROS signalling in the biology of cancer, Semin. Cell Dev. Biol. 80 (2018) 50–64.
[30] M.J. Seo, D.M. Lee, I.Y. Kim, D. Lee, M.K. Choi, J.Y. Lee, S.S. Park, S.Y. Jeong, E. K. Choi, K.S. Choi, Gambogic acid triggers vacuolization-associated cell death in cancer cells via disruption of thiol proteostasis, Cell Death Dis. 10 (2019) 187.
[31] C.Y. Wu, L.T. Zhou, H.B. Yuan, S.Y. Wu, Interconnections among major forms of regulated cell death, Apoptosis 25 (2020) 616–624.
[32] I. Cakir, E.A. Nillni, Endoplasmic reticulum stress, the hypothalamus, and energy balance, Trends Endocrinol. Metab. 30 (2019) 163–176.
[33] A. Fernández, R. Ordóñez, R.J. Reiter, J. González-Gallego, J.L. Mauriz, Melatonin and endoplasmic reticulum stress: relation to autophagy and apoptosis, J. Pineal. Res. 59 (2015) 292–307.
[34] C. Lebeaupin, D. Vallée, Y. Hazari, C. Hetz, E. Chevet, B. Bailly-Maitre, Endoplasmic reticulum stress signalling and the pathogenesis of non-alcoholic fatty liver disease, J. Hepatol. 69 (2018) 927–947.
[35] Q. Liu, H. Körner, H. Wu, W. Wei, Endoplasmic reticulum stress in autoimmune diseases, Immunobiology 225 (2020), 151881.
[36] S.A. Oakes, Endoplasmic reticulum stress signaling in cancer cells, Am. J. Pathol. 190 (2020) 934–946.
[37] S.A. Oakes, F.R. Papa, The role of endoplasmic reticulum stress in human pathology, Annu. Rev. Pathol. 10 (2015) 173–194.
[38] Z.H. Qi, L.X. Chen, Endoplasmic reticulum stress and autophagy, Adv. Exp. Med. Biol. 1206 (2019) 167–177.
[39] M.Q. Zhu, M.D. Yang, J.J. Zhang, Y.Z. Yin, X. Fan, Y. Zhang, S.S. Qin, H. Zhang, F. Yu, Immunogenic cell death induction by ionizing radiation, Front Immunol. 12 (2021), 705361.
[40] J.Y. Zhou, G.Y. Wang, Y.Z. Chen, H.X. Wang, Y.Q. Hua, Z.D. Cai, Immunogenic cell death in cancer therapy: present and emerging inducers, J. Cell Mol. Med. 23 (2019) 4854–4865.
[41] X.W. Wang, S.W. Wu, F. Liu, D.S. Ke, X.W. Wang, D.L. Pan, W.F. Xu, L. Zhou, W. D. He, An immunogenic cell death-related classification predicts prognosis and response to immunotherapy in head and neck squamous cell carcinoma, Front Immunol. 12 (2021), 781466.
[42] T. Verfaillie, A.V. Vliet, A.D. Garg, M. Dewaele, N. Rubio, S. Gupta, P. Witte, A. Samali, P. Agostinis, Pro-apoptotic signaling induced by photo-oxidative ER stress is amplified by Noxa, not Bim, Biochem. Biophys. Res. Commun. 438 (2013) 500–506.
[43] R.D.W. Vaes, L.E.L. Hendriks, M. Vooijs, D.D. Ruysscher, Biomarkers of radiotherapy-induced immunogenic cell death, Cells 10 (2021) 930.
[44] H. Ruan, B.J. Leibowitz, L. Zhang, J. Yu, Immunogenic cell death in colon cancer prevention and therapy, Mol. Carcinog 59 (2020) 783–793.
[45] L. Minute, A. Teijeira, A.R. Sanchez-Paulete, M.C. Ochoa, M. Alvarez, I. Otano, I. Etxeberrria, E. Bolaños, A. Azpilikueta, S. Garasa, N. Casares, J.L.P. Gracia, M. E. Rodriguez-Ruiz, P. Berraondo, I. Melero, Cellular cytotoxicity is a form of immunogenic cell death, Cancer Res. 80 (2020).
[46] Y.H. Li, X.H. Liu, X. Zhang, W. Pan, N. Li, B. Tang, Immunogenic cell death inducers for enhanced cancer immunotherapy, Chem. Commun. 57 (2021) 12087–12097.
[47] G. Kroemer, C. Galassi, L. Zitvogel, L. Galluzzi, Immunogenic cell stress and death, Nat. Immunol. 23 (2022) 487–500.
[48] T.L. Whiteside, FOXP3^{+} Treg as a therapeutic target for promoting anti-tumor immunity, Expert Opin. Ther. Tar. 22 (2018) 353–363.
[49] A. Tanaka, S. Sakaguchi, Targeting Treg cells in cancer immunotherapy, Eur. J. Immunol. 49 (2019) 1140–1146.
[50] A. Tanaka, S. Sakaguchi, Regulatory T cells in cancer immunotherapy, Cell Res. 27 (2017) 109–118.
[51] Y. Ohue, H. Nishikawa, Regulatory T (Treg) cells in cancer: Can Treg cells be a new therapeutic target, Cancer Sci. 110 (2019) 2080–2089.
[52] A.M. Leun, D.S. Thommen, T.N. Schumacher, CD8^{+} T cell states in human cancer: insights from single-cell analysis, Nat. Rev. Cancer 20 (2020) 218–232.
[53] L.M. McLane, M.S. Abdel-Hakeem, E.J. Wherry, CD8 T cell exhaustion during chronic viral infection and cancer, Annu. Rev. Immunol. 37 (2019) 457–495.
[54] W.X. Huff, J.H. Kwon, M. Henriquez, K. Fetcko, M. Dey, The evolving role of CD8^{+}CD28^{-} Immunosenescent T cells in cancer immunology, Int. J. Mol. Sci. 20 (2019) 2810.
[55] C.Y. Li, M.X. Yu, Y. Sun, Y.Q. Wu, C.H. Huang, F.Y. Li, A nonemissive iridium(III) complex that specifically lights-up the nuclei of living cells, J. Am. Chem. Soc. 133 (2011) 11231–11239.
[56] Y.M. You, S.Y. Park, Inter-ligand energy transfer and related emission change in the cyclometalated heteroleptic iridium complex: facile and efficient color tuning over the whole visible range by the ancillary ligand structure, J. Am. Chem. Soc. 127 (2005) 12438–12439.
[57] M. Nonoyama, Benzo[h]quinolin-10-yl-N iridium(III) complexes, Chem. Soc. Jpn. 47 (1974) 767–768.